

# Supplementary Appendix

## Contents

<b>CONTENTS</b> .....	<b>1</b>
<b>LIST OF INVESTIGATORS AND CONTRIBUTIONS</b> .....	<b>3</b>
<b>SUPPLEMENTAL TEXT</b> .....	<b>4</b>
<b>S1 – EXPERIMENTAL PROCEDURES</b> .....	<b>4</b>
S1.01 – CLINICAL PROTOCOL AND STUDY PARTICIPANT .....	4
S1.02 – MULTI-MODAL MRI-BASED MOTOR LOCALIZATION.....	4
S1.03 – SURGICAL PLANNING .....	5
S1.04 – IMPEDANCE MEASUREMENT.....	6
S1.05 – BRAIN-COMPUTER INTERFACE TRAINING PARADIGMS .....	6
S1.06 – HAND TRAJECTORY RECOGNITION IN THE FREE GRASPING PARADIGMS.....	7
<b>S2 – RIEMANNIAN DECODER</b> .....	<b>7</b>
S2.01 – SPATIO-SPECTRAL RIEMANNIAN GEOMETRY DECODING METHOD.....	7
S2.02 – CONTROL DECODING METHODS.....	9
S2.03 – DECODING CONTINUOUS GRASPING STATES USING HIDDEN MARKOV MODEL .....	10
S2.04 – MODEL TRAINING AND EVALUATION .....	10
<b>S3 – OFFLINE ANALYSIS</b> .....	<b>11</b>
S3.01 – COMPARISON OF THREE TYPES OF BRAIN ELECTROPHYSIOLOGY RECORDINGS .....	11
<b>S4 – REHABILITATION</b> .....	<b>12</b>
S4.01 – SEP MEASUREMENT.....	12
S4.02 – SCALES MEASUREMENT .....	13
<b>SUPPLEMENTAL FIGURES</b> .....	<b>14</b>
FIGURE S1 MRI SCANS OF THE PATIENT'S HEAD AND NECK.....	14
FIGURE S2 fMRI LOCALIZATION PARADIGM AND SURGICAL PLANNING.....	15
FIGURE S3 BRAIN-COMPUTER INTERFACE DECODING METHODS.....	16
FIGURE S4 ILLUSTRATION OF HMM DECODING. ....	17
FIGURE S5 CALIBRATION AND TRAINING PARADIGMS. ....	18
FIGURE S6 CHANGES IN EPIDURAL ECOG FEATURE DISTRIBUTION DURING LONG-TERM Use. ....	19
FIGURE S7 EMG NOISE PATTERN.....	20
FIGURE S8 AVERAGE SOMATOSENSORY EVOKED POTENTIAL (SEP) WAVEFORMS. ....	21
FIGURE S9 SEP AMPLITUDE CHANGES OVER TIME.....	22
FIGURE S10 PNEUMATIC HAND KEYPOINT DETECTION MODEL. ....	23

<b>SUPPLEMENTAL TABLES</b> .....	<b>24</b>
TABLE S1: ISNCSCI SCORES .....	24
TABLE S2: P-VALUES FOR INCREASES IN AVERAGE AMPLITUDES.....	25
TABLE S3: ARAT SCORES.....	26
<b>REFERENCE</b> .....	<b>27</b>

# List of investigators and contributions

## List of investigators (authors):

1. Dingkun Liu\*
2. Yongzhi Shan\*
3. Penghu Wei\*
4. Wenzheng Li
5. Honglai Xu
6. Fangshuo Liang
7. Tao Liu
8. Guoguang Zhao
9. Bo Hong

\* These authors contributed equally

## Author contributions:

# Supplemental Text

## S1 – Experimental procedures

### S1.01 – Clinical Protocol and Study Participant

This study was approved by the ethics committee of Xuanwu Hospital of Capital Medical University in April 2023 and registered for international clinical trials of implanted medical devices (NCT05920174) to conduct research on the implanted closed-loop brain-computer interface system (NEO). The surgery was performed at Xuanwu Hospital, with other related studies conducted at Tsinghua University and the patient's home. Our study includes three main phases: preoperative functional screening, surgery, a one-month calibration and adjustment period, and an eight-month BCI assisted active rehabilitation training period. The rehabilitation training involved a total of 100 sessions, each lasting 1-3 hours, personalized according to the patient's progress. In the 9<sup>th</sup> month, the training load was doubled to maximize the patient's recovery outcomes.

The participant is a male in his 50s who sustained a spinal cord injury more than 10 years due to a car accident. The participant signed a written informed consent before participation. Moreover, the participant gave his consent for the material depicting himself to appear in the contribution and to be published in the journal and associated works without limit on the duration of publication, in any form or medium.

Before the surgery, the patient underwent a neurological impairment assessment, currently diagnosed as a complete C4 spinal cord injury (ASIA-A, Extended Data Table 1). The patient's muscle tone was rated at level 2-3 on the Modified Ashworth Scale (MAS), indicating an increase in muscle tone that affects passive movement within the range of motion. The patient reported taking Baclofen (10mg/day) and Pregabalin (75mg/day) to relieve spasms at the sixth month post-surgery. This symptom has persisted since the injury and is unrelated to the BCI implant.

TODO: EEG test

### S1.03 – Multi-modal MRI-based Motor Localization

Before the implantation surgery, the subject underwent a head MRI on a 3.0T scanner (Siemens, Prisma) to locate brain areas associated with hand sensory and motor functions. Functional MRI (fMRI) was acquired using a gradient echo planar imaging (EPI) sequence with the following parameters: matrix size 100×100, resolution 2×2×2 mm<sup>3</sup>, repetition time (TR) 2 s, echo time (TE) 30 ms. The scan covered the entire brain with 72 slices. T1-weighted MRI structural images were acquired using a magnetization-prepared rapid gradient-echo (MPRAGE) sequence with parameters: matrix size 256×256, resolution 1×1×1 mm<sup>3</sup>, and 208 slices.

The fMRI paradigm was used to locate the subject's sensorimotor areas related to hand movement. The paradigm consisted of two parts. The first part involved passive movement, where two experimenters assisted the subject with passive fist clenching on the left and right sides at a frequency of approximately 0.5 Hz. This was designed to test whether sensory information could be transmitted to the cortex, indicating the condition of the subject's ascending pathways. The second part involved motor imagery, where the subject was asked to imagine moving their left or right hand in a familiar manner. This was used to locate the hand motor areas in the primary motor (M1) and primary sensory (S1) cortices. The block design included two alternating conditions: movement and rest. At the beginning of the movement condition, an arrow pointing left or right appeared on the screen with a text prompt to "start imagining left hand/right hand movement." At the beginning of the rest condition, an image of a teacup appeared with a text prompt to "rest, relax, stay calm," instructing the subject to remain relaxed during this period. Each condition lasted 14 seconds (7 TRs, yielding 7 fMRI frames), repeated for 14 cycles. The left- and right-hand conditions alternated with a rest condition in between (Extended Data Fig. 2).

## S1.04 - Surgical Planning

Based on the results of the functional MRI activations, we developed a surgical implantation plan for the subject. Using the fMRI activation heatmaps combined with anatomical localization of the hand motor and sensory areas, we performed 3D modeling to select specific sites on the precentral and postcentral gyri for the right hand, where epidural cortical electrodes were placed to cover regions of significant fMRI activation (Extended Data Fig. 2). The internal device was implanted into the flat skull behind the ear, ensuring sufficient bone thickness, avoiding the temporalis muscle, and facilitating wireless charging.

To effectively integrate the electrode positioning from the surgical plan with the surgical navigation system, a novel engineering method was developed to address compatibility issues between the 3D model and the navigation system. The cortex was segmented using FreeSurfer<sup>1</sup>, and an individualized cortical model of the patient's brain was constructed. The electrode placement on the cortical surface was designed in Blender to cover the functional areas of the precentral and postcentral gyri. To import the positioning results into the surgical navigation system, we wrote the electrode locations into the patient's original T1 DICOM data. This process involved coordinate transformation between FreeSurfer's Surface RAS reference frame and the image's original RAS reference frame (Equation 1).

$$X' = AX \quad 1$$

where  $X$  represents the homogeneous coordinates of the electrode points in the Surface RAS reference frame  $(x, y, z, 1)$ ,  $X'$  represents the new coordinates in the original RAS reference frame  $(x', y', z')$ , and  $A$  is the transformation matrix  $(3 \times 4)$  converting from the FreeSurfer's Surface RAS coordinate system to the DICOM image's scanner RAS coordinate system. An optimized kd-tree nearest neighbor algorithm was used to efficiently map these coordinates to the pixel points in the original DICOM images. In this setup, all pixels within a 1mm radius were marked with a value significantly higher than the maximum MRI intensity (e.g., 5000). The modified DICOM files were then imported into the navigation system, allowing the surgeon to directly determine the electrode positions during surgery. The final electrode implantation sites, as shown in Fig. 1d, matched the planned locations and the areas of optimal fMRI activation.

## S1.05 - Impedance Measurement

The NEO system supports impedance measurement using milliampere (mA) stimulation current. The system uses a stimulation current of 1 mA with a pulse width of 1000  $\mu$ s at a pulse frequency of 10 Hz for a duration of 5000 ms. It measures the impedance between the epidural electrode contacts. Once a month, we record impedance data to track the trend of internal environment change (Fig. 2g).

## S1.06 - Brain-Computer Interface Training Paradigms

The calibration task is utilized for personalized model calibration and BCI testing. The paradigm consists of 15 trials per session, with each trial including 5 seconds of movement, feedback (10 seconds for success, 2 seconds for failure), and 5 seconds of resting state. The experiment begins with a 10-second period during which a crosshair appears at the center of the screen, and the participant needs to focus on the crosshair and remain calm. After 10 seconds, the actual task begins. At the start of the motor imagery task, a one second blank screen is firstly given to remind the participant to prepare. After that, an arrow pointing left or right appears at the center of the screen, indicating left-hand or right-hand movement respectively, accompanied by a text prompt "Start imagining left-hand/right-hand movement." Feedback is provided after the motor phase, with the model making a judgment every second during the 5-second motor phase. The task has three difficulty levels: easy, medium, and hard, requiring correct judgments of 3, 4, and 5 times respectively. Only with correct judgments will the participant receive pneumatic hand feedback and a "Congratulations" message on the screen; otherwise, the message "Keep trying" will be displayed (Extended Data Fig. 5a). Before fixing the model, random feedback with an 85% accuracy rate is given. In the first session of the calibration paradigm, fake feedback is used. In the second calibration session, feedback results are calculated using the model calibrated with the first session of training data. After the second calibration session, the final model is trained using data from both sessions and fixed for the patient. We perform this calibration task monthly to periodically assess the model's performance.

During rehabilitation training, the patient uses the fixed model for free grasping tasks. The model makes a judgment every 0.1 seconds to determine the patient's grasping or relaxation state. To avoid false triggers caused by the EEG offset response after the patient's releasing an object, there is a 3-second freeze period during which no new judgments are made. The model displays the confidence level of the grasp in the form of a progress bar on the screen, providing visual feedback to the participant. To quantitatively evaluate the effectiveness of the BCI system, we designed a **nine-square grid paradigm** requiring the patient to take objects to designated targets using the BCI. A 50.4 cm wide and 35.6 cm long nine-square grid board, as well as standard components of height 15 cm, upper cylinder diameter 4.5/6/6.5 cm, and lower disc diameter 10 cm were used in this paradigm (Extended Data Fig. 5b). The patient is instructed by the experimenter to use the BCI to drive the pneumatic hand to grasp the standard component from the center of the nine-square grid and move it to the designated color block position, then release the object by controlling the pneumatic hand. The test is repeated in two rounds, and the total time from the

start of the instruction to the successful placement of the object is recorded to evaluate whether the patient can smoothly control the state switching of the BCI system. We also compared the patient's success rate with and without BCI assistance. Success is defined as completing the task within 10 seconds without touching the grid boundaries before picking up the object and without dropping it midway. Any other result is considered a failure.

## S1.07 - Hand Trajectory Recognition in the Free Grasping paradigms

To accurately capture hand movement trajectories during the free grasping process, a USB webcam was positioned directly above the experimental table to record the hand movements from a top-down perspective (Extended Data Fig. 10). A serial port synchronization signal and LED light were used to synchronize the video recording with the EEG data. For the video data of both pneumatic hand grasping and bare hand grasping, we finetuned a hand keypoint detection model to analyze the hand movement trajectories. The main structure of the model utilizes a high-resolution convolutional network (HRNet)<sup>12</sup> pre-trained on the OneHand10k dataset. The detection algorithm employs distribution-aware coordinate representation (DARK)<sup>13</sup> based on heatmaps to detect four key points of the pneumatic hand or the hand: the index fingertip, thumb tip, the base of the thumb (thenar), and the wrist. For the patient's grasping data, the coordinates of the thenar key point were extracted as the hand movement trajectory. The start time of each trial was defined as the moment the hand contacted the central cylindrical object, and the end time was defined as the moment of grasping failure or successfully reaching the target position and releasing the object. The model was fine-tuned based on the OneHand10K pre-trained model. The pneumatic hand model training data included 1,295 annotated images with a resolution of 960x540, with 80% of the data used for training and 20% for testing. The keypoint recognition model achieved an AUC of 0.89. The bare hand detection model training data included 1,118 annotated images with a resolution of 960x540, with 80% of the data used for training and 20% for testing. The model achieved an AUC of 0.85.

## S2 – Riemannian Decoder

### S2.01 - Spatio-Spectral Riemannian Geometry Decoding Method

The spatio-spectral information in eECoG signals can be described using a covariance matrix. Typical eECoG responses to motor imagery include ERSP across different frequency bands. By constructing a multi-band joint covariance matrix (Equation 3), we can effectively extract the spatio-spectral patterns of the EEG:

$$C_f = \begin{pmatrix} Z_{f_1} Z_{f_1}^T & \dots & Z_{f_1} Z_{f_F}^T \\ \vdots & \ddots & \vdots \\ Z_{f_F} Z_{f_1}^T & \dots & Z_{f_F} Z_{f_F}^T \end{pmatrix} \quad 3$$

where  $Z_{f_i}, i = 1, \dots, F$  represents the channel signals filtered by different frequency bands, and  $F$  is the number of selected frequency bands.

The Affine Invariant Riemannian Metric (AIRM, Equation 4) can measure the distance between covariance matrices:

$$\delta_r(C_1, C_2) = \left\| C_1^{-1/2} C_2 C_1^{-1/2} \right\|_F = \left( \sum_{i=1}^n \log^2 \lambda_i \right)^{1/2} \quad 4$$

where  $\|\cdot\|_F$  represents the Frobenius norm, and  $\lambda_i$  are the eigenvalues of the matrix  $C_1^{-1/2} C_2 C_1^{-1/2}$ .

The AIRM metric has the following property: for any two samples from the source space that form covariance matrices  $S_A$  and  $S_B$ , mapping through a propagation matrix  $L$  (where  $L$  is invertible) results in sensor space covariance matrices  $X_A = L S_A L^T$ ,  $X_B = L S_B L^T$ . It can be proven that:

$$\delta_r(X_A, X_B) = \delta_r(S_A, S_B)$$

This indicates that the separability in the source space and the sensor space is identical. Similarly, over long-term use, physiological changes may alter the propagation matrix  $L'$ , but the AIRM distance measure ensures that separability remains unchanged. In contrast, BCI decoding algorithms using spatial filters may fail due to changes in the propagation matrix, causing spatial filter templates to become ineffective. Therefore, BCI decoding algorithms using the AIRM metric possess robustness in the sensor space and long-term stability.

To select the most effective frequency bands for decoding, we evaluated the separability of different frequency bands for resting and right-hand motor imagery states using a Riemannian-based class distinctiveness method.

Linear Discriminant Analysis (LDA) can be extended to construct class distinctiveness metrics under the Riemannian metric (Equation 5)<sup>5</sup>:

$$D(A, B) = \frac{\delta_r(\overline{C^A}, \overline{C^B})}{\frac{1}{2}(\sigma_{C^A} + \sigma_{C^B})} \quad 5$$

where  $\overline{C}$  represents the mean covariance under the Riemannian metric, and  $\sigma_C$  represents the standard deviation of the covariance under the Riemannian metric,  $\sigma_C = \frac{1}{n-1} \sum_{i=1}^n \delta_r(C_i, \overline{C})$ . The superscripts  $C^{(A/B)}$  indicate the corresponding classes.



Subsequently, a classifier based on AIRM can be constructed by embedding the data into the tangent space<sup>6</sup>. For the manifold  $M$  constituted by the aforementioned eCoG feature covariance matrices, the Fréchet mean point  $X_{ref}$  of the manifold can be found (Equation 6):

$$X_{ref} = \operatorname{argmin}_{X_{ref}} \sum_{i=1}^N \delta^2(X_i, X_{ref}) \quad 6$$

Based on this point, the tangent space  $T_{X_{ref}}M$  can be constructed, and the data points  $X_i$  can be embedded into this space to obtain the projected points  $S_i$  (Equation 7), where  $\log_m$  denotes the matrix logarithm operation.

$$S_i = \log_{X_{ref}}(X_i) = X_{ref}^{-\frac{1}{2}} \log_m \left( X_{ref}^{-\frac{1}{2}} X_i X_{ref}^{-\frac{1}{2}} \right) X_{ref}^{-\frac{1}{2}} \quad 7$$

In our study, the epidural intracranial EEG of patients exhibits a typical Event Related Synchronization (ERS) effect at high frequencies (e.g., 55-95Hz) and a typical Event Related Desynchronization (ERD) effect at low frequencies (15-30Hz and 35-50Hz). Therefore, we designed a dual-frequency integrated spatio-spectral Riemannian geometry algorithm. Due to the physiological differences between low-frequency and high-frequency oscillatory activities, low-frequency activities were filtered at 15-30Hz and 35-50Hz, while high-frequency activities were band-pass filtered at 55-95Hz and then enveloped (Extended Data Fig. 3). Subsequently, a large covariance matrix of the feature signals was constructed, which was whitened to retain 99% of the variance dimension components to reduce the dimensionality. The samples were then embedded into the tangent space constituted by the Fréchet mean point, and finally sent to a logistic regression classifier to build the decoder for BCI calibration.

## S2.02 - Control Decoding Methods

We employed two classical BCI decoding methods to evaluate our model. **Linear Model:** To evaluate the decoding method proposed in this paper, we selected a commonly used linear model as a baseline for comparison<sup>7,8</sup>. This linear model first uses a band-pass filter in the 0-150Hz frequency range to filter the signal into nine different frequency bands and then downsamples to 10Hz. The signals from the nine frequency bands and different channels are then concatenated into a 315-dimensional feature vector (7 channels \* 9 frequency bands \* 5 time points). Finally, this feature vector is used for decoding with a logistic regression classifier. We also used 10-fold cross-validation to optimize the regularization parameter of the logistic regression classifier to prevent overfitting. **Common Spatial Pattern (CSP) Model:** Additionally, since there is a close relationship between Riemannian methods and spatial filtering methods, we designed a model using CSP spatial filters to compare with the Riemannian method's results<sup>9,10</sup>. This model constructs the covariance matrix using the same frequency bands as the Riemannian method. The CSP method is then used to calculate and retain 16 spatial filters. The energy features of the resulting 16-dimensional spatial patterns are used for decoding with a logistic regression classifier.

For each model, 10-fold cross-validation is used to optimize the regularization parameter of the logistic regression classifier to prevent overfitting.

## S2.03 - Decoding Continuous Grasping States using Hidden Markov

### Model

Considering that the natural grasping process is inherently continuous, with each state at a given time point being dependent on the preceding and following states, leveraging this dependency can significantly enhance the reliability of maintaining a grasp. The Hidden Markov Model (HMM), by constructing a multi-order stochastic process, links the probability of the current hidden state with the observed data and the probability of the hidden state at the previous time point. This can be used to describe the natural grasping process. We define the hidden states as either resting or grasping. In our constructed HMM algorithm, the emission probability  $p(z_t|s_k)$  is derived from the Riemannian geometric classification model obtained through supervised training, while the transition probability matrix is semi-supervised, estimated using the forward-backward algorithm based on data from the patient's free-grasping training sessions. The first-order Hidden Markov Model can predict the probability of each hidden state at the current step based on the probability of each hidden state at the previous step (Equation 8):

$$p(s_{k,t}) = p(z_t|s_k) \sum_i p(s_{k,t}|s_{i,t-1})p(s_{i,t-1}) \quad 8$$

where  $z_t$  is the observed data at time  $t$ , and  $s_k$  is state  $k$ . We set a threshold  $p_{th}$ , and when the likelihood probability of the patient's new state exceeds this threshold, the model switches states. This threshold is estimated based on offline validation results and is set to 0.8 for the patient.

Additionally, we apply an extra step of first-order filtering to smooth the probabilities output by the HMM (Equation 9). The parameter  $\eta$  is adjusted based on offline validation results and is set to 0.7 for the patient.

$$\hat{p}_{curr} = \eta p_{last} + (1 - \eta)p_{curr} \quad 9$$

where  $p_{last}$  is the hidden state probability from the previous step,  $p_{curr}$  is the current hidden state probability inferred from Equation 6, and  $\hat{p}_{curr}$  is the final estimated hidden state probability.

## S2.04 - Model Training and Evaluation

The model is trained based on two sets of calibration data. Since High Gamma (HG) activity decays over time during imagined grasping, we use data from the first 1.5 seconds after the onset of motor imagery and the entire 5 seconds of resting state as the training data. The data are segmented at 0.5-second intervals for model fitting. One set of data is used for model training,

utilizing 10-fold cross-validation to select the optimal regularization parameters for the classifier. After fitting the classification model, we fit the HMM state transition matrix using the patient's grasping behavior data to construct a complete decoding model. Validation is conducted using a different set of data, evaluating both segment metrics and event metrics. After validation, a final model is trained using both sets of calibration data.

During model calibration, it is necessary to design evaluation criteria to assess the effectiveness of the model. Since the goal is to decode natural grasping states, which is a continuous time process, evaluation needs to consider both segment metrics (such as sample classification accuracy) and event metrics (sensitivity and specificity of event detection). **Segment Metrics:** The model directly classifies data segments and calculates classification accuracy. Additionally, due to the uneven distribution of classes in the segmented data samples, the F1 score (the harmonic mean of precision and recall) is used, which is insensitive to class imbalance. For segment metrics, the random level for the F1 score and AUC is 0.5. **Event Metrics:** To evaluate grasping accuracy over continuous time, we designed event-based metrics. If a grasping event is correctly identified within 0.5s before its onset and 2 seconds after it, it is considered a correct judgment; otherwise, it is a false negative. If more than one grasping event is detected during a single grasping event, it is considered a false positive. Precision, recall, and their harmonic mean (F1 score) are calculated accordingly. Due to the low frequency of grasping events, the random level for event metrics is low. Monte Carlo simulations estimate the random level for the F1 score of event metrics to be approximately 0.09 (with the grasping onset time covered about 10% of total time), indicating that continuous grasping tasks are relatively difficult, much harder than simple binary classification tasks.

## S3 - Offline Analysis

### S3.01 - Comparison of Three Types of Brain Electrophysiology

#### Recordings

To compare the differences between epidural electrocorticography (eECoG) and subdural electrocorticography (sECoG), we utilized data from the publicly available Kai Miller dataset<sup>2</sup>. Since the motor imagery patterns of paralyzed patients are more similar to actual movements in healthy individuals<sup>3</sup>, we selected real hand movement data from 10 patients whose electrodes covered the hand area. The cortical electrodes in the Kai Miller dataset had a spacing of 10 mm and a contact diameter of 2.3 mm. In our study, we used electrodes with a spacing of 8 mm and a contact diameter of 3.2 mm, which are comparable in size. The EEG electrode spacing in the patients' EEG caps was approximately 4 cm. To ensure consistent results, all three types of brain electrical activity were processed using the common average rereference method. Additionally, to study the spatial resolution differences between different brain recordings, we introduced motor imagery data from the BCI2000 dataset for comparison<sup>4</sup>.

In terms of frequency, we calculated the Event-Related Spectral Perturbation (ERSP) for eECoG, sECoG, and EEG during the 0-2.5 seconds of movement relative to the 0-2.5 seconds of resting state (Equation 2). This allowed us to compare the modulation depths of different frequency bands across the different brain electrical activities.

$$ERSP = \frac{P_{task} - P_{rest}}{P_{rest}} \quad 2$$

Where  $P_{task}$  refers to the power of the brain electrical activity in the frequency band during movement, and  $P_{rest}$  refers to the power in the resting state. Power spectral density (PSD) was calculated using resting state data to compare the spectral energy differences of the different brain electrical activities (Fig. 2b).

To qualitatively compare the spatial resolution differences, we calculated the relationship between the distance between electrode pairs and the correlation coefficient of the electrode signals (Fig. 2c). To maintain consistency with the number of subjects and tasks selected in the eECoG dataset, we selected all electrode pairs from the first 10 subjects in the BCI2000 dataset for real left- and right-hand movements. All eECoG signals were filtered with a 1 Hz high-pass filter, using the original reference electrodes (EEGs were referenced to mastoids, sECoGs and eECoGs were referenced to the scalp).

## **S4 – Rehabilitation**

### **S4.01 – SEP Measurement**

The testing of somatosensory evoked potentials (SEP) follows the standards of the International Federation of Clinical Neurophysiology (IFCN)<sup>11</sup>. The stimulation sites are at the wrist corresponding to the median, radial and ulnar nerves respectively. A 6×9 cm silver/silver chloride adhesive electrode is used. The positive electrode is placed distally on the trunk, the negative electrode proximally, with a 2 cm distance between them. The stimulation is a unidirectional pulse, with 2 Hz frequency 400 μs pulse width and amplitudes of 16 mA for the median and radial nerves, or 12 mA for the ulnar nerve. This setup aims to stably evoke SEP while avoiding pain. The stimulation is repeated 160 times in each session. During stimulation, SEPs are recorded with epidural electrodes at a sampling rate of 1000 Hz. The signals are band-pass filtered (20-400 Hz) and averaged across trials to obtain the SEP waveform. Monthly recordings are repeated at the same stimulation site and parameters to observe changes in the SEP waveform.

In SEP analysis, for early (15-35 ms) and late (40-80 ms) SEP components, the average waveform amplitude is extracted. To minimize amplitude increases due to enhanced random phase oscillatory activity, the Bootstrap method is used. For each Bootstrap sample set, the average SEP response is extracted, and the average waveform amplitudes of early and late components are extracted. For the data from 1<sup>st</sup> and 9<sup>th</sup> month after implantation, permutation test is used to

calculate the p-values that 9<sup>th</sup> month's amplitude is greater than that of 1<sup>st</sup> month, and the FDR correction is applied to control the false discovery rate in multiple comparisons.

## S4.02 – Scales Measurement

This study uses the ISNCSCI scale and the ARAT scale to assess patients' neurological and upper limb functional status, respectively. The ISNCSCI scale is evaluated by two attending physicians, and any discrepancies in their evaluations are discussed to reach a single result. The ISNCSCI scale is measured monthly starting from the 2<sup>nd</sup> to 9<sup>th</sup> month post-surgery. The ARAT scale assessments are conducted by rehabilitation physicians and experimenters, with the process being video recorded.

## Supplemental Figures

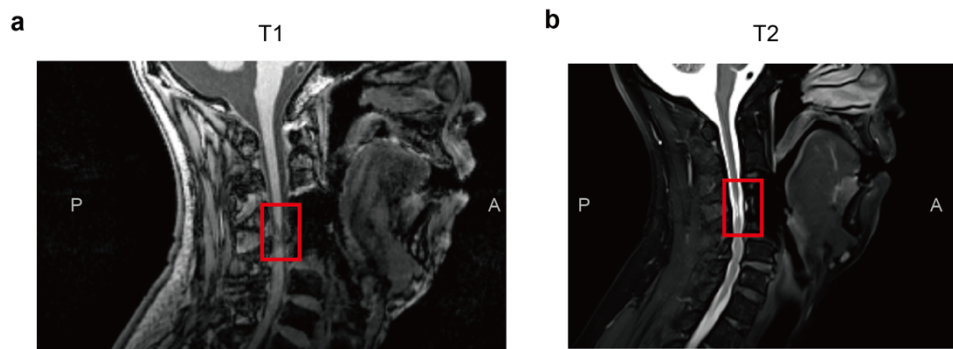


Figure S1 MRI Scans of the Patient's Head and Neck.

a, Cervical spine T1 structural image b, Cervical spine T2 structural image; the red box indicates the location of the patient's spinal cord injury.

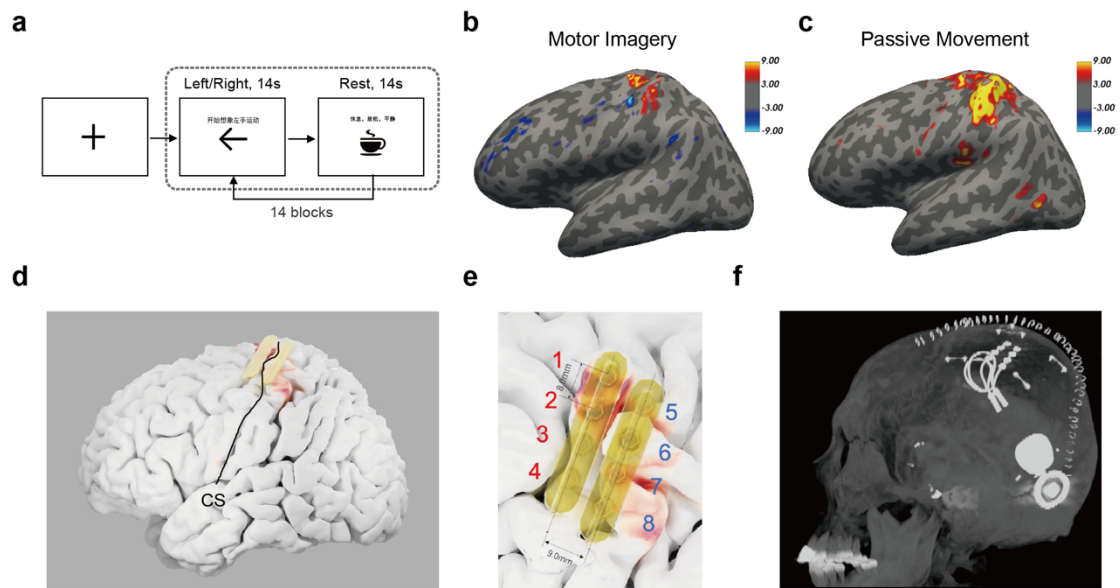


Figure S2 fMRI Localization Paradigm and Surgical Planning.

a, fMRI functional localization paradigm, including alternating rest and movement states of the left or right hand. b-c, Functional activation during motor imagery (b) and passive movement (c), with activation values represented as  $-\lg(p)$ . d, Electrode planning. e, Enlarged view of the diagram of the planned electrodes. Electrodes 1-4 were located on the precentral gyrus and electrodes 5-8 on the postcentral gyrus. f, Sagittal View of postoperative CT, showing the actual implantation positions. CS: Central Sulcus.

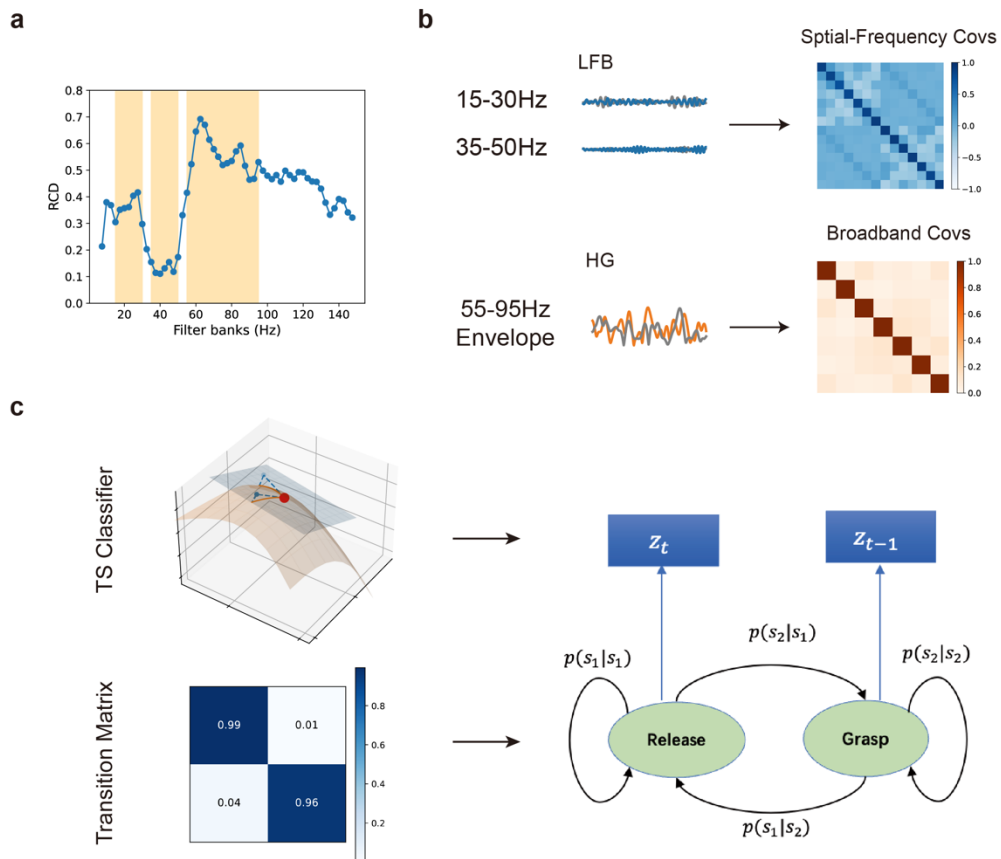


Figure S3 Brain-Computer Interface Decoding Methods.

a, Band selection using Riemannian class distinctiveness (RCD) across different frequency bands. b, Construction of the covariance feature matrix using low-frequency band-pass filter features and high-frequency envelope features. c, Decoding framework for natural grasping based on the Hidden Markov Model (HMM), utilizing the temporal dependence of grasp states to ensure the reliability of continuous grasping. The observation model is based on the trained Riemannian geometry classifier, and the transition matrix is fitted based on patient behavior data. TS Classifier: Tangent Space Classifier.



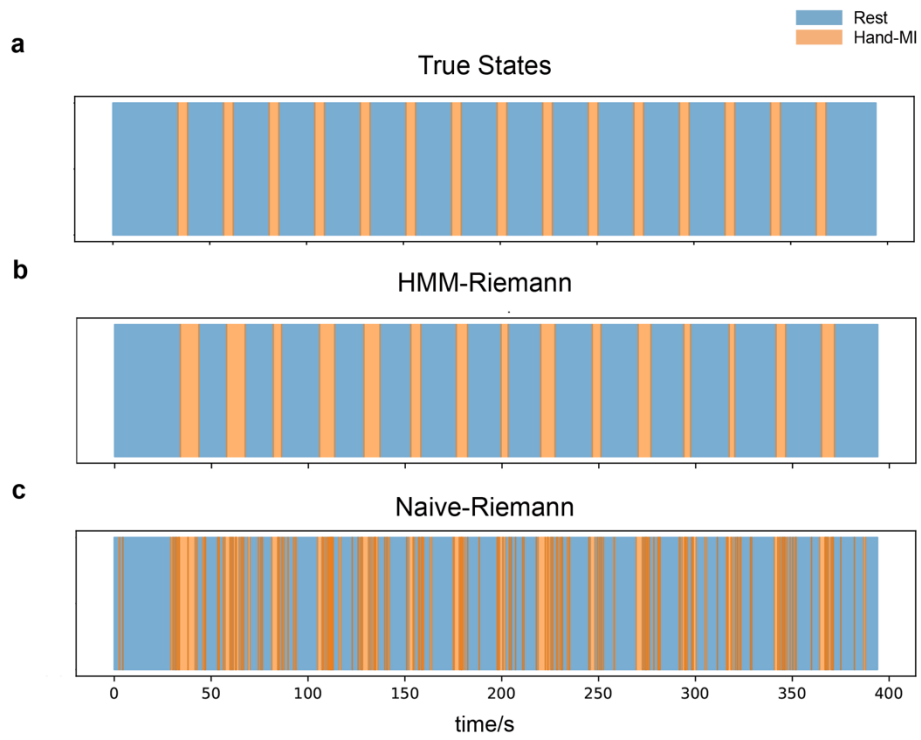


Figure S4 Illustration of HMM decoding.

a, Actual motor imagery cues. b, Continuous grasping decoded by the HMM-Riemann method. c, Continuous grasping decoded by the Naïve-Riemann method without HMM. Hand-MI: Hand Motor Imagery.

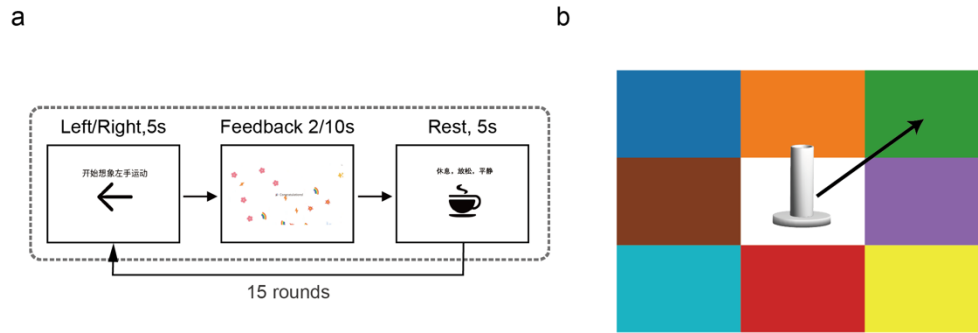


Figure S5 Calibration and Training Paradigms.

a, BCI calibration paradigm. b, Free grasp BCI testing paradigm, where the patient needs to move the standard cylinder from the center to the grid designated by the experimenter.

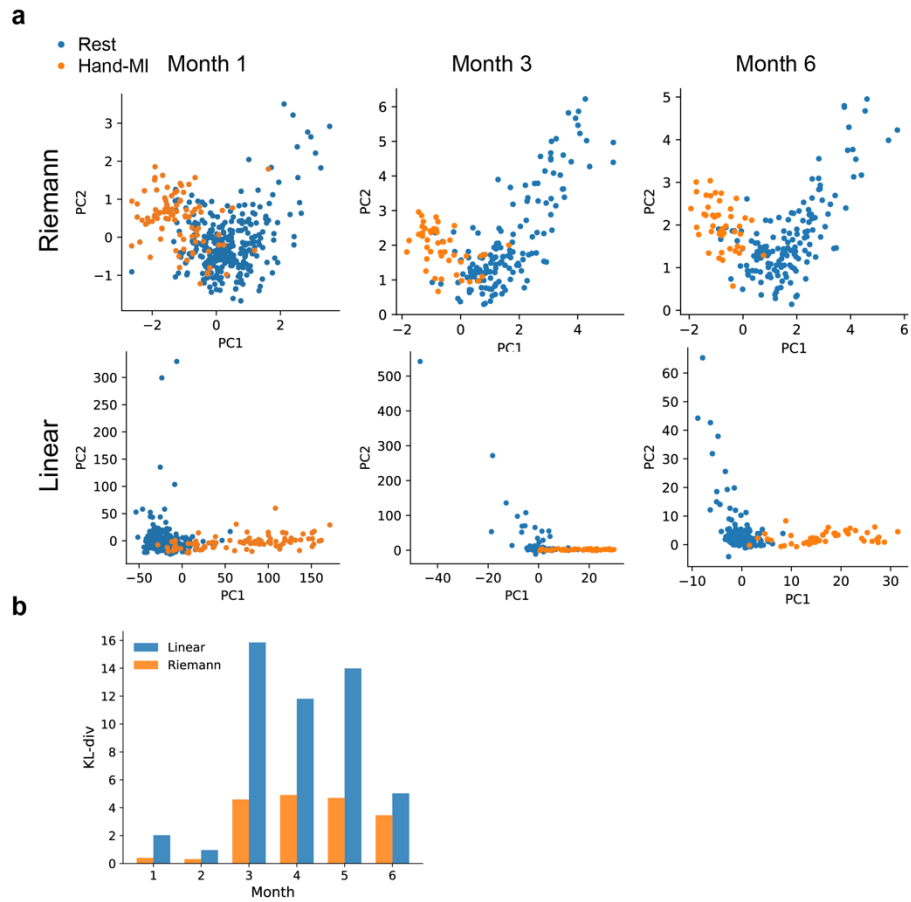


Figure S6 Changes in epidural ECoG Feature Distribution During Long-term Use.

a, Scatter plots of PCA-embedded distributions of Riemannian features and linear spatio-temporal-spectral features across different months. b, Changes in KL divergence between Riemannian features and linear spatio-temporal-spectral features compared to training data over different months. The stability of Riemannian features consistently surpasses that of linear spatio-temporal-spectral features. Hand-MI: Hand Motor Imagery. KL-div: KL Divergence.

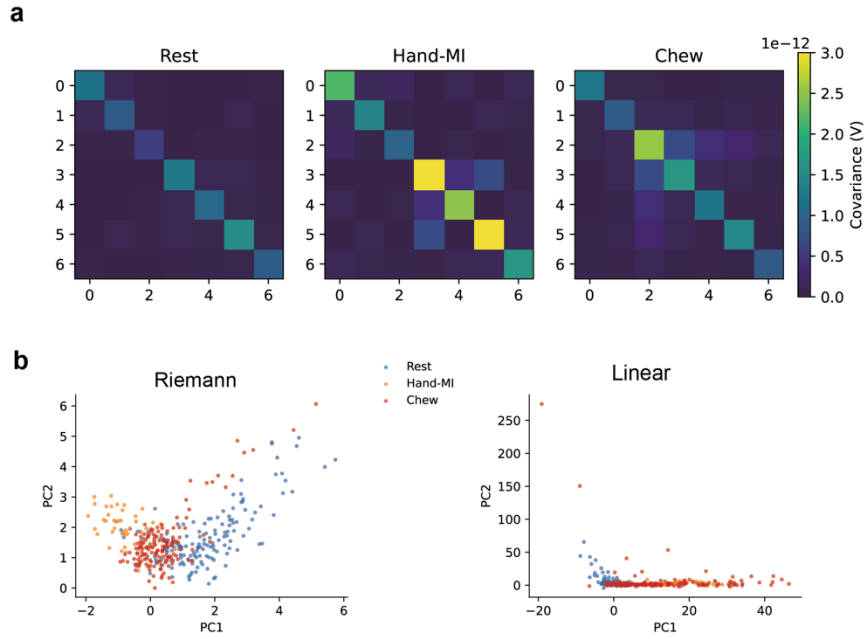


Figure S7 EMG Noise Pattern.

a, Average covariance patterns of resting, motor imagery (Hand-MI), and EMG noise. b, Dimensionality-reduced spatial distribution patterns of Riemannian embedded features (left) and linear spatio-temporal-spectral features (right). Under Riemannian metrics, chewing EMG noise is positioned between resting and hand motor imagery; in linear spatio-temporal-spectral features, chewing noise highly overlaps with hand motor imagery distribution.

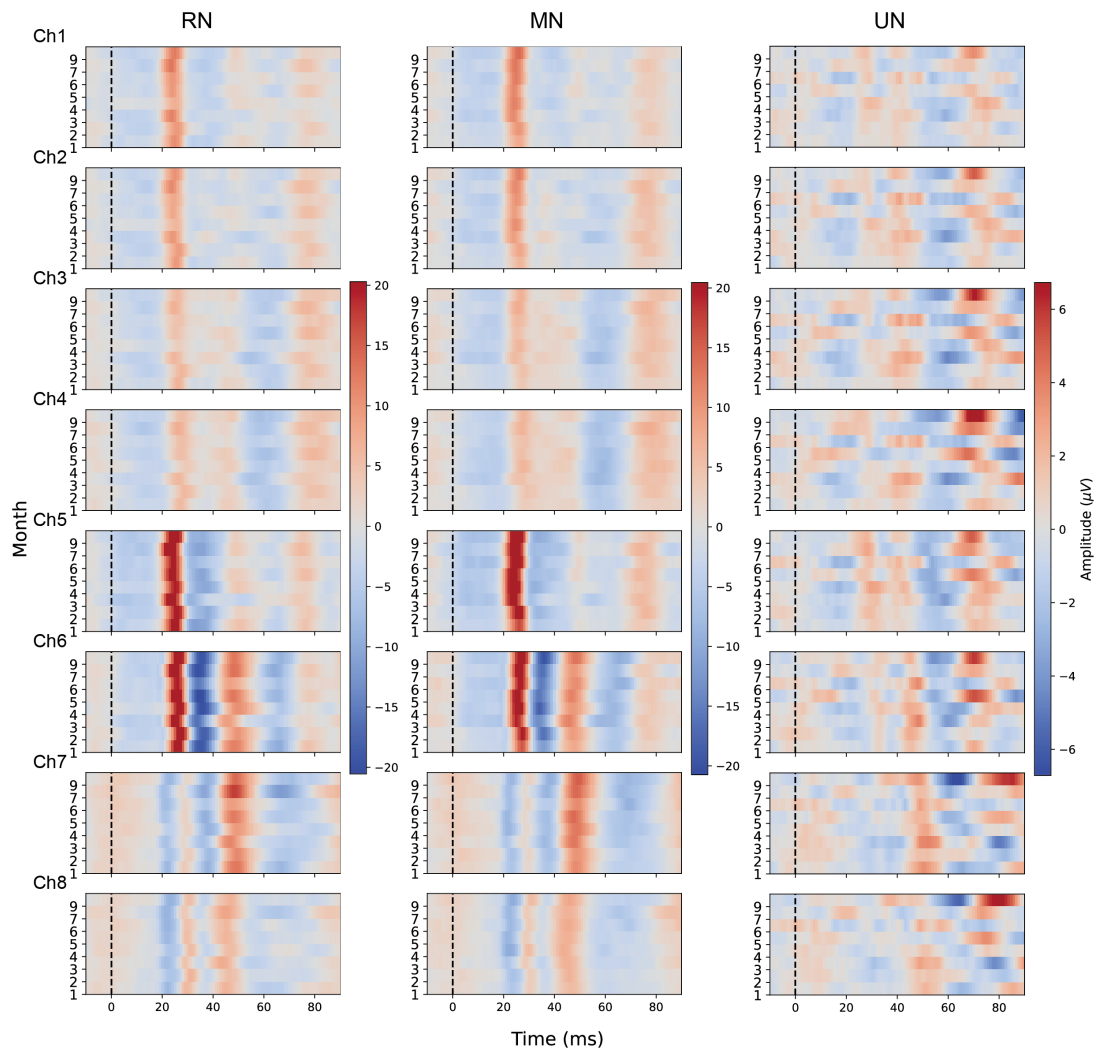


Figure S8 Average Somatosensory Evoked Potential (SEP) Waveforms.  
 Average SEPs for Each Nerve, Channel, and Month. From top to bottom: Ch1-Ch8.

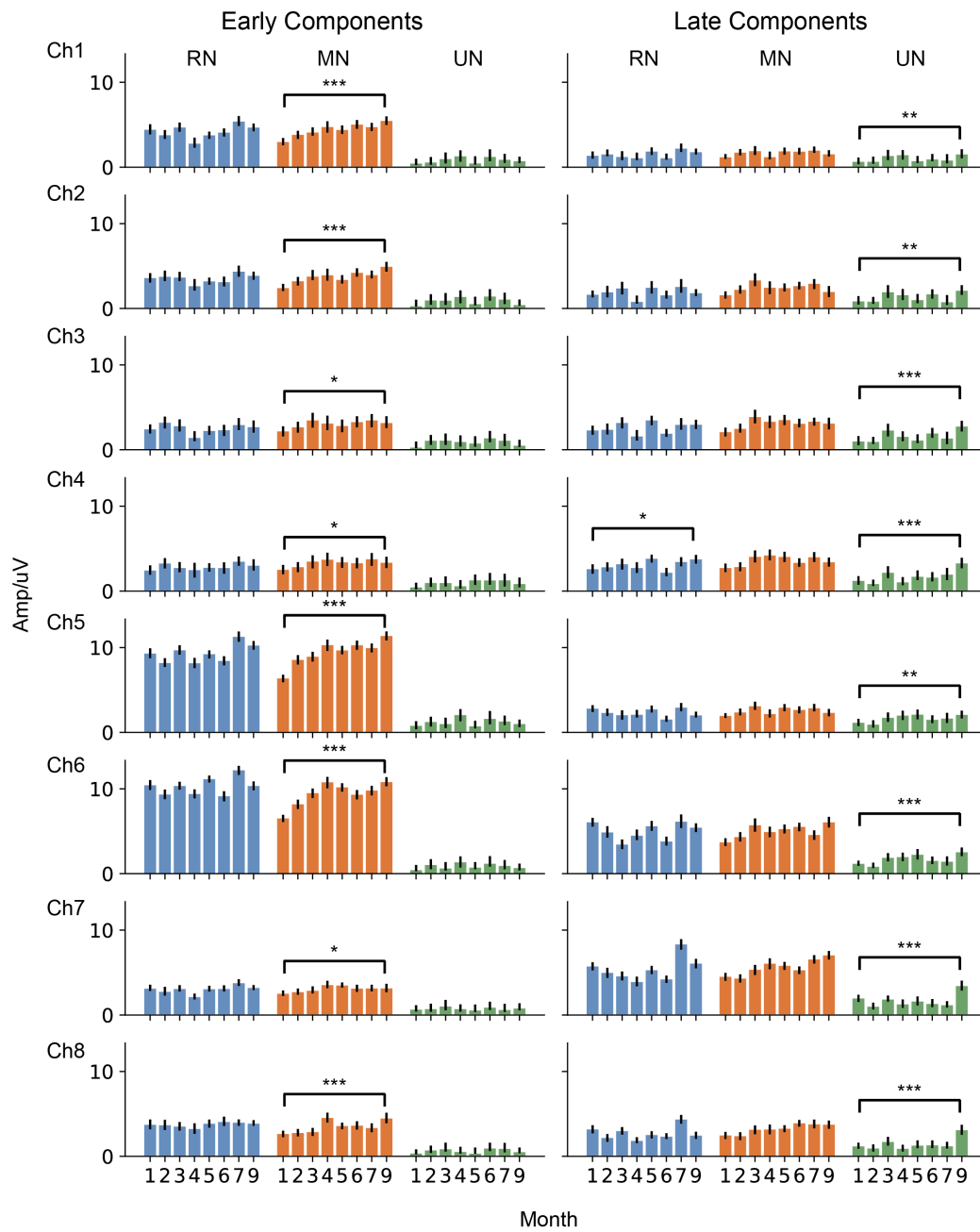
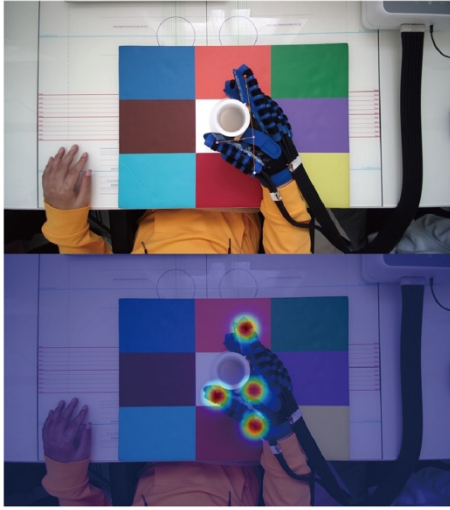


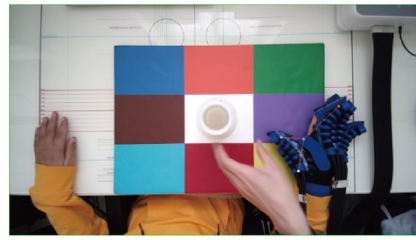
Figure S9 SEP amplitude changes over time.

Relationship of average amplitude changes over time for early SEP components (15-35 ms, top) and late SEP components (40-80 ms, bottom) for Each Nerve, Channel, and Month. From top to bottom: Ch1-Ch8. \*:  $p < 0.05$ , \*\*:  $p < 0.01$ , \*\*\*:  $p < 0.001$ , bootstrap permutation test.

**a**



**b**



**c**



Figure S10 Pneumatic Hand Keypoint Detection Model.

a, Example of a detection heatmap. b-c, Examples of detection results.

# Supplemental Tables

Table S1: ISNCSCI Scores

Time	Pre-Operation	Month 3	Month 4	Month 5	Month 6	Month 7	Month 9
American Spinal Injury Association Impairment Scale (AIS)	A	A	A	A	A	A	A
Neurological level of injury	C4	C4	C4	C4	C4	C4	C4
Upper Extremity Motor Score							
C5, (Left   Right)	4   4	4   4	4   5	4   5	4   5	4   5	5   5
C6, (Left   Right)	3   3	3   3	3   3	3   4	3   3	3   3	3   4
C7, (Left   Right)	2   2	2   2	2   3	2   2	2   2	2   3	2   3
C8, (Left   Right)	0   0	0   0	0   0	0   0	0   0	1   0	0   1
T1, (Left   Right)	0   0	0   0	0   0	0   0	0   0	0   0	0   0
Total, (Left   Right)	9   9	9   9	9   11	9   11	9   10	10   11	10   13
Light Touch Sensory Score							
Total, (Left   Right)	7   8	9   7	8   9	11   9	7   7	7   7	7   7
Pin Prick Sensory Score							
Total, (Left   Right)	6   7	10   8	10   8	11   8	10   9	11   10	11   11
Deep Anal Pressure	No	No	No	No	No	No	No
Voluntary Anal Contraction	No	No	No	No	No	No	No



Table S2: p-values for Increases in Average Amplitudes.

	RN		MN		UN	
	Early	Late	Early	Late	Early	Late
Ch1	0.2461	0.0901	<0.0001	0.0746	0.1579	0.0069
Ch2	0.2369	0.2654	<0.0001	0.1905	0.3035	0.0007
Ch3	0.2555	0.0479	0.0235	0.0119	0.2198	<0.0001
Ch4	0.1068	0.0021	0.0396	0.0381	0.1161	<0.0001
Ch5	0.0078	0.9957	<0.0001	0.1021	0.2586	0.0013
Ch6	0.5814	0.9572	<0.0001	<0.0001	0.1724	<0.0001
Ch7	0.3704	0.184	0.0176	<0.0001	0.3169	0.0001
Ch8	0.3518	0.9889	<0.0001	0.0001	0.2373	<0.0001

Compared between SEP data from month 1 and month 9 of Early and Late SEP Components for Different Nerves.

Table S3: ARAT scores

	Baseline		Month 3		Month 5		Month 7		Month 9	
	L	R	L	R	L	R	L	R	L	R
<b>Grasp (18)</b>	6	4	5	6	6	10	6	9	12	13
<b>Grip (12)</b>	6	6	6	6	6	6	6	6	7	10
<b>Pinch (18)</b>	2	2	2	2	4	4	3	4	5	6
<b>Gross (9)</b>	7	9	8	9	8	8	8	8	8	8
<b>Total (57)</b>	21	21	21	23	24	28	23	27	32	37

## Reference

1. Fischl, B. FreeSurfer. *Neuroimage* **62**, 774–781 (2012).
2. Miller, K. J. A library of human electrocorticographic data and analyses. *Nat. Hum. Behav.* **3**, 1225–1235 (2019).
3. Lotze, M. & Halsband, U. Motor imagery. *J. Physiol. Paris* **99**, 386–395 (2006).
4. Schalk, G., McFarland, D. J., Hinterberger, T., Birbaumer, N. & Wolpaw, J. R. BCI2000: A General-Purpose Brain-Computer Interface (BCI) System. *IEEE Trans. Biomed. Eng.* **51**, 1034–1043 (2004).
5. Yamamoto, M. S., Lotte, F., Yger, F. & Chevallier, S. Class-distinctiveness-based frequency band selection on the Riemannian manifold for oscillatory activity-based BCIs: preliminary results. in *2022 44th Annual International Conference of the IEEE Engineering in Medicine & Biology Society (EMBC)* vols 2022-July 3690–3693 (IEEE, 2022).
6. Barachant, A., Bonnet, S., Congedo, M. & Jutten, C. Classification of covariance matrices using a Riemannian-based kernel for BCI applications. *Neurocomputing* **112**, 172–178 (2013).
7. Benabid, A. L. *et al.* An exoskeleton controlled by an epidural wireless brain–machine interface in a tetraplegic patient: a proof-of-concept demonstration. *Lancet Neurol.* **18**, 1112–1122 (2019).
8. Moly, A. *et al.* An adaptive closed-loop ECoG decoder for long-term and stable bimanual control of an exoskeleton by a tetraplegic. *J. Neural Eng.* **19**, (2022).
9. Koles, Z. J. The quantitative extraction and topographic mapping of the abnormal components in the clinical EEG. *Electroencephalogr. Clin. Neurophysiol.* **79**, 440–447 (1991).
10. Lemm, S., Blankertz, B., Curio, G. & Müller, K. R. Spatio-spectral filters for improving the classification of single trial EEG. *IEEE Trans. Biomed. Eng.* **52**, 1541–1548 (2005).
11. Cruccu, G. *et al.* Recommendations for the clinical use of somatosensory-evoked potentials. *Clin. Neurophysiol.* **119**, 1705–1719 (2008).
12. Wang, J. *et al.* Deep High-Resolution Representation Learning for Visual Recognition. *IEEE Trans. Pattern Anal. Mach. Intell.* **43**, 3349–3364 (2021).
13. Zhang, F., Zhu, X., Dai, H., Ye, M. & Zhu, C. Distribution-Aware Coordinate Representation for Human Pose Estimation. *Proc. IEEE Comput. Soc. Conf. Comput. Vis. Pattern Recognit.* 7091–7100 (2020) doi:10.1109/CVPR42600.2020.00712.